CHEMISTRY OF MATERIALS

Article

pubs.acs.org/cm

Structural and Chemical Evolution of Amorphous Nickel Iron Complex Hydroxide upon Lithiation/Delithiation

Kai-Yang Niu,[†,∥] Feng Lin,[‡,∥] Liang Fang,[†,§,∥] Dennis Nordlund,[⊥] Runzhe Tao,[†] Tsu-Chien Weng,[⊥] Marca M. Doeff,[†] and Haimei Zheng*[,†,¶]

[†]Materials Sciences Division and [‡]Environmental Energy Technologies Division, Lawrence Berkeley National Laboratory, Berkeley, California 94720, United States

[§]State Key Laboratory of Mechanical Transmission, College of Physics, Chongqing University, Chongqing 400044, People's Republic of China

[⊥]Stanford Synchrotron Radiation Lightsource, SLAC National Accelerator Laboratory, Menlo Park, California 94025, United States

[¶]Department of Materials Science and Engineering, University of California, Berkeley, California 94720, United States

Supporting Information

ABSTRACT: Development of novel electrode materials is essential to achieve high-performance lithium ion batteries. Here, we demonstrate that amorphous nickel iron complex hydroxides (Ni−Fe−OH) synthesized by a laser−chemical method can be used as a potential conversion anode material for lithium storage. Complementary characterizations, including ensemble-averaged X-ray absorption spectroscopy, spatially resolved electron energy-loss spectroscopy, and energy dispersive X-ray spectroscopy in a scanning transmission electron microscope, were performed to reveal the chemical and structural evolutions of the active hydroxide particles undergoing electrochemical cycling. The solid−electrolyte interphase (SEI) layer with a primary component of lithium fluoride (LiF) was found and remained robust on the particle surface during the charge/discharge processes, which suggests that the LiF-containing SEI layer plays a critical role in maintaining the stable capacity retention and good reversibility of the Ni−Fe−OH anode.

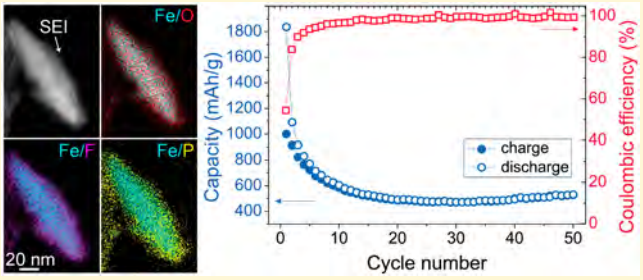

INTRODUCTION

There is an ever increasing demand for rechargeable batteries with high energy density and outstanding cyclability for portable and mobile electronics in the modern technological world.[1] After many years' competition with the nickel−cadmium and nickel−metal hydride rechargeable batteries, lithium ion batteries (LIBs) have become the fastest growing and most promising solution for superior energy storage.[1−3] The development of advanced electrode materials for lithium storage has been one of the central missions for building high-performance LIBs.[1,4,5] To this end, the pursuit of high energy density conversion reaction materials has been a major research thrust in the battery community.[4,6,7] Up to date, a series of transition metal compounds (i.e., M_aX_b, where M = Fe, Co, Ni, Mn, Co, Cr, Ti, etc., and X = O, S, N, P, and F) have shown intriguing lithium storage properties,[4,8−15] among which transition metal hydroxides as electrode materials for LIBs have been less commonly reported. Achievements have been obtained in using the composites of hydroxide and graphene as LIB anode materials such as $Ni(OH)_2$/graphene[16,17] and $Co(OH)_2$/graphene.[18,19] However, pristine hydroxide anodes often suffer severe and continual capacity fading,[16] which results in a low cyclability of the electrode.

Herein, we demonstrate that an amorphous nickel iron complex hydroxide (Ni−Fe−OH) exhibits improved lithium storage capability compared to other hydroxides and a stable capacity retention of 540 mAh/g maintained over 50 cycles, which makes it a possible conversion electrode material for the LIB. In this paper, we aim to study the chemical and structural transformation of the Ni−Fe−OH nanostructures and the evolution of solid−electrolyte interphase (SEI) layer to reveal the fundamental mechanisms of improved lithium storage performance during the lithiation/delithiation processes. Characterizations, that is, soft X-ray absorption spectroscopy (XAS), electron energy-loss spectroscopy (EELS), and energy dispersive X-ray spectroscopy (EDS) in a scanning transmission electron microscope (STEM), were carried out.[8,20−22] SiO_2 thin film-supported transmission electron microscopy (TEM) copper grids, loaded with a small amount of the active material, were pressed against the bulk anode and assembled into the coin cells; the active materials were collected at different states of the charge/discharge process for characterizations where the

Received: November 10, 2014
Revised: January 23, 2015
Published: January 27, 2015

DOI: 10.1021/cm5041375
Chem. Mater. 2015, 27, 1583−1589

electrodes were used for soft XAS and copper grids for STEM-EELS/EDS.

A facile laser−chemical method was adopted to synthesize the Ni−Fe−OH compound where laser irradiating a precursor solution leads to the growth via hydrolysis reactions of metal ions (Figure 1a, and see the reaction mechanism in Supporting Information). We used a Continuum Surelite III nanosecond pulsed laser with the laser wavelength, pulse energy, and frequency of 1064 nm, 750 mJ/pulse, and 10 Hz, respectively. The precursor solution is an aqueous mixture of nickel nitrate and iron nitrate. Figure 1, panel b shows that the clear green reactant solution turned darker and darker after laser irradiation, and a brown particulate suspension was finally produced, from which a brown powder of Ni−Fe−OH was isolated after collecting, rinsing, and drying.

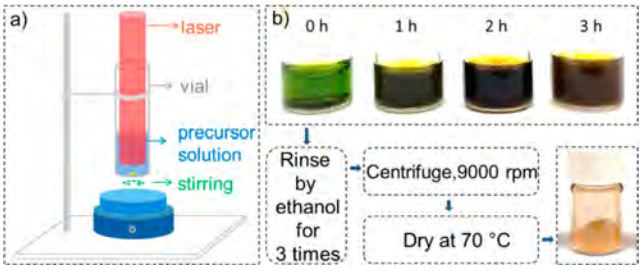

Figure 1. (a) Schematic diagram of laser synthesis in solution. (b) Photographs of the solution at different stages of laser irradiation. The subsequent process for obtaining the powder product for lithium storage is highlighted.

EXPERIMENTAL SECTION

Laser−Chemical Synthesis of the Amorphous Nickel Iron Complex Hydroxide Nanostructures. A Continuum SureliteIII nanosecond pulsed laser was used as a power source, which has four different wavelengths: 1064 nm, 532 nm, 355 nm, and 266 nm. The typical laser parameters of operation are 1064 nm wavelength, 10 Hz frequency, 7−8 ns pulse width, 0.9 cm beam diameter, and 980 mJ per pulse. Aqueous solutions of 1 M nickel nitrate and 1 M iron nitrate were prepared as precursors. For synthesis in water, 3 h laser irradiation (pulse energy of 700 mJ) was applied for a 4 mL mixed precursor solution with Ni:Fe molar ratio of 1:1. Precipitates produced by laser irradiation were rinsed by ethanol and centrifuged at 9000 r/min and repeated for three times, then dried in air at 70 °C to obtain a powder product. All chemicals including nickel nitrate (99.99%) and iron nitrate (98%) were purchased from Sigma-Aldrich and used as received. The deionized water was produced by Milli-Q integral water purification system.

Battery Coin Cell Fabrication and Test. Composite electrodes were prepared with 70 wt % active material, 15 wt % polyvinylidene fluoride (PVDF), and 15 wt % acetylene carbon black in *N*-methyl-2-pyrrolidone (NMP) and cast onto copper current collectors with loadings of 2−3 mg/cm^2. Two-thousand thirty-two coin cells were assembled in a helium-filled glovebox using the composite electrode as the positive electrode and Li metal as the negative electrode. A Celgard separator 2400 and 1 M LiPF6 electrolyte solution in 1:1 w/w ethylene carbonate/diethyl carbonate were used to fabricate coin cells. Battery testing was performed on computer controlled VMP3 channels (BioLogic). 1C was defined as discharging the nickel iron complex hydroxide with a specific capacity of 720 mAh/g in 1 h. The charging current was set identical to that of the discharging in the present study. Electrochemical impedance spectra were collected after full cycles with a 10 mV AC signal ranging from 10−100 kHz.

Characterizations. TEM was used for structural and morphology characterization. EELS was acquired using a Gatan Tridiem spectrometer equipped on 200 kV FEI monochromated F20 UT Tecnai TEM. An EDS spectrum was obtained using 200 kV TitanX TEM equipped with the windowless SDD Bruker EDS detectors with fast processor and FEI Double-tilt Ultratwin Low background sample holder.

TA Instruments Q5000IR TGA-MS was used for the thermal gravimetric analysis (TGA); argon gas was used with a flow rate of 25 mL/min, and the temperature was ramped to 600 °C at a rate of 5 °C/min for testing. PerkinElmer Spectrum One Fourier transform infrared (FT-IR) with HATR assembly was used for FT-IR measurements. X-ray diffraction (XRD) on powder samples was performed on a Bruker D2 Phaser diffractometer using Cu−Kα radiation.

High-throughput soft XAS measurements were performed on the 31-pole wiggler beamline 10−1 at Stanford Synchrotron Radiation Lightsource (SSRL) using a ring current of 350 mA and a 1000 L mm^{-1} spherical grating monochromator with 20 μm entrance and exit slits, which can provide 10^{11} ph s^{-1} at 0.2 eV resolution in a 1 mm two beam spot. During the measurements, all samples were attached to an aluminum sample holder, and the surface was connected to the isolated holder using conductive carbon. Data were acquired in a single load at room temperature and under ultrahigh vacuum (10^{-9} Torr). Detection was performed in total electron yield (TEY) mode (with probing depth of ~5 nm), where the sample drain current was normalized by the current form of a reference sample in a form of freshly evaporated gold on a thin grid positioned upstream of the sample chamber.

RESULTS AND DISCUSSION

Figure 2 displays the chemical and structural information on the as-synthesized Ni−Fe−OH complex hydroxide. The STEM images and EDS maps show that the Ni−Fe−OH nanostructures have a homogeneous distribution of Ni, Fe, O, and N (Figure 2a). The broad peaks in the XRD pattern (Figure 2b)

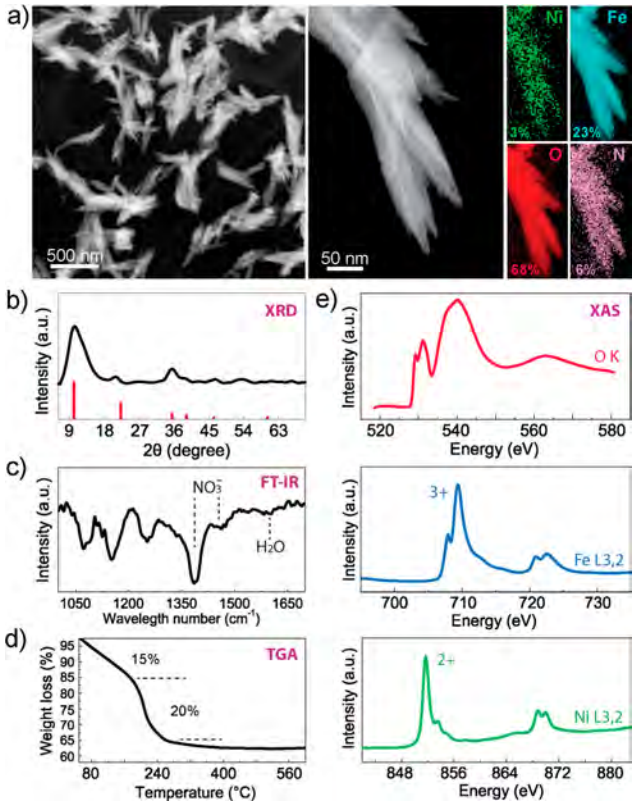

Figure 2. (a) STEM images and EDS mapping of the as-prepared Ni−Fe−OH nanostructures. (b) XRD, (c) FT-IR, and (d) TGA analyses of the Ni−Fe−OH nanostructures. (e) XAS spectra (total electron yield mode, TEY) of O K-edge, Fe L-edge, and Ni L-edge, respectively.

DOI: 10.1021/cm5041375
Chem. Mater. 2015, 27, 1583−1589

indicate that the Ni−Fe−OH compound has a low crystallinity (amorphous-like, compared with the crystalline structure of nickel iron layered double hydroxide,[23] shown as line markers in Figure 2b) with nitrate ions and water molecules located between the layers (Figure 2c). The TGA (Figure 2d) shows a 35% weight loss of the material below about 240 °C, corresponding to a 15% loss of absorbed and structurally bonded water and a 20% loss due to the evolution of H_2O and NO_2.[24]

Soft XAS was used to determine the valence states of the metal ions in the as-prepared powder (Figure 2e). The Fe L-edge and Ni L-edge spectra show that in the pristine material, the oxidation states are 3+ for Fe and 2+ for Ni, respectively.[8,25,26] The detailed interpretation of O K-edge XAS was complicated due to the unknown characteristics in the local ionic ordering as well as the possible contribution of bound water and nitrate ions. However, the lowest energy state near 530 eV can be unambiguously associated with Fe 3d−O 2p hybridized states. We associate the second feature in the pre-edge with the expected doublet peak of Fe^{3+} hybridized states (similar to Fe_2O_3), overlapped with a smaller intensity from the Ni 3d−O 2p states.[8,27,28] On the basis of the intensity of the pre-edge relative to the main edge, we conclude that the spectrum is dominated by oxygen in the metal hydroxide with some contribution from other oxygen functionalities, for example, water and nitrate ions (note that neither water nor nitrate ions have XAS features below 534 eV). On the basis of the structure and elemental analyses, we formulate the as-synthesized amorphous nickel iron hydroxide as $[Ni_{0.1}Fe_{0.9}(OH)_2](NO_3)_x \times mH_2O$ (where x and m could be estimated from the EDS quantification and TGA analysis as 0.2 and 1.0, respectively).

The pristine Ni−Fe−OH compound was cycled as the active material in a half-cell configuration using lithium metal as the counter electrode. The capacity−voltage profile in Figure 3, panel a shows that the material delivered a charge capacity of 1000 mAh/g in the first cycle after undergoing an initial discharge. The cell then underwent continual fading until the 20th cycle, after which a stable capacity of ∼540 mAh/g was maintained. A slight enhancement of the charge/discharge capacity was observed after 30 cycles. Although there was an obvious Coulombic inefficiency at the first cycle (Figure 3b), because of the presence of side reactions, such as irreversible electrolyte decomposition, dissolution of the active material, and formation of SEI layer, the Coulombic efficiency was drastically improved after the first cycle and approached 100% after 20 cycles (Figure 3b). The electrochemical impedance spectra (EIS, Figure 3c) show that the charge transfer resistance of the electrode undergoes minor change after 50 cycles (increases from 142 Ohm to 200 Ohm), which indicates excellent stability of the electrode for battery cycling. There is an increase of mass transfer resistance attributable to the passivation by electrolyte decomposition products, as described later in the text. Overall, the cycling performance of the amorphous Ni−Fe−OH nanostructures is comparable to commonly reported metal oxides and hydroxides as the anode materials.[4,15,16]

With the grids-in-coin-cells methodology, four coin cells loaded with TEM grids were prepared for battery testing, and the active materials were transferred in argon gas protection and taken out for characterizations at five charge/discharge states, that is, pristine, 50% discharged, fully discharged, 50%

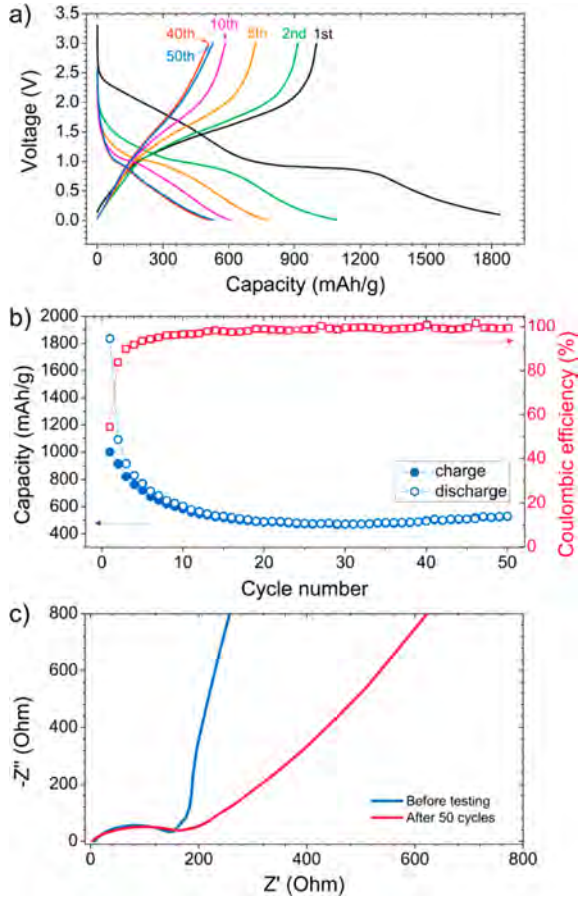

Figure 3. (a) Charge−discharge voltage profile (at C/2 rate), (b) capacity retention (left y-axis), and (c) Coulombic efficiency (right y-axis) of lithium half cells using the as-prepared Ni−Fe−OH nanostructures as anode materials.

charged, and fully charged states (see Figure S1a, Supporting Information).

The XAS/TEY was used to study the electrode−electrolyte interfacial phenomenon. Because of the limited mean free path of electrons in the materials, XAS/TEY (with probing depth of ∼5 nm) offers a means to probe the surface chemical environment. Figure 4, panel a shows the XAS evolution of the Fe L-edge, where a dramatic decrease of the absolute intensity was detected during the first discharge, which suggests the formation of an SEI layer on active material particle surfaces, which did not contain Fe. The SEI layer evolved over the first cycle but did not fully decompose after a full cycle, and the valence states of Fe and Ni ions were reversible, which stayed as Fe^{3+} and Ni^{2+} after one cycle (Figure 4a and Figure S1b). We also note the emergence of strong F 1s XAS intensity at lower energies with a shoulder near 700 eV and an increasing extended X-ray absorption fine structure (EXAFS) oscillation characteristic near 715 eV (marked as triangle in Figure 4a), which suggest the existence of LiF in the SEI layer.[29] Figure 4, panel b displays the drastic changes of the XAS O K-edge. The pre-edge of the O K-edge, associated with (Ni, Fe) 3d−O 2p hybridization (see Figure 2 and associated text), vanished at the 50% discharged state, which is consistent with the Fe L-edge intensity loss. Instead, a sharp peak at higher energy, indicative of a π^* resonance, such as in carbonyl functionalities [π^*(C═O)], dominates the pre-edge structure, from which we can associate this feature primarily with carbonate species,[8,30]

DOI: 10.1021/cm5041375
Chem. Mater. 2015, 27, 1583−1589

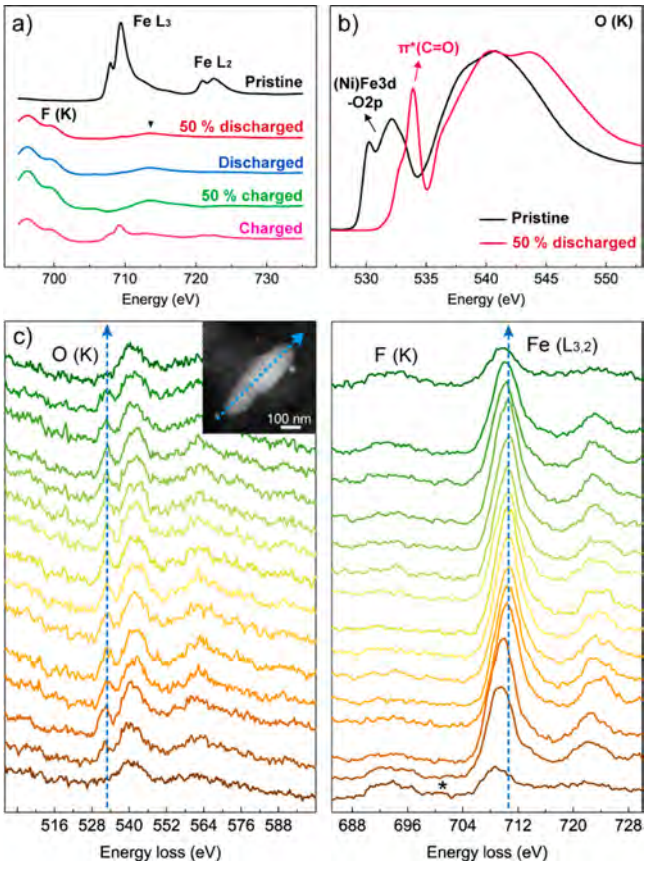

Figure 4. (a) XAS/TEY spectra of Fe L-edge and F K-edge for electrodes at five different states of charge, that is, pristine (black), 50% discharged (red), discharged (blue), 50% charged (green), and one cycle charged (pink) states. The triangle symbol marks the EXAFS feature attributable to LiF in the SEI layer. The XAS intensity of Fe L-edge at the pristine state is reduced by three times for demonstration. (b) XAS/TEY O K-edge spectra for electrodes in the pristine state (black) and in the 50% discharged state (blue), and the assignment of peaks is indicated in the figure. (c) EELS spectra of Fe L-edge and O K-edge across a Ni−Fe−OH nanostructure in the 50% discharged state. Inset is the STEM image of the nanostructure, and the blue dashed arrow shows the path of the EELS line scan. The star symbol marks a shoulder feature attributable to LiF.

although other remains of electrolyte species cannot be excluded. Further analysis and elemental identification of the SEI layer were investigated using spatially resolved STEM-EELS spectroscopy.

Figure 4, panel c shows the line scan EELS spectra of the Fe L-edge, F K-edge, and O K-edge on a particle in the 50% discharged state. Obvious shifts of the Fe L-edge are observed over its length. The rightward shifting of the Fe L-edge from the surface to the center is as large as 2 eV, and the pre-edge of the O K-edge does not show up on the surface, which indicates that the Fe ions have been reduced to Fe^0, but Fe^{3+} is still maintained inside the particle due to the incomplete reduction.[31] The high intensity of the F K-edge on the particle surface indicates that a F-containing species covers the surface; the subtle shoulder close to the F K-edge (marked with a star) implies that LiF might have formed on the surface,[32] which is consistent with the observation of the EXAFS feature of LiF in Figure 4, panel a (marked with a triangle).

Figure 5 shows the structure determination of the active particles in the fully discharged state. The STEM-EELS line scan over a thin nanostructure (Figure 5a) indicates that the LiF phase exists on the particle surface. The slight shifts (from the center to the edge) of the Fe L_3 edge indicate that iron ions are at lower oxidation states, likely Fe^0 species, since no obvious pre-edge of the O K-edge is observed. Figure 5, panel b demonstrates relatively large particles that are embedded in the reaction species, from which an obvious SEI layer over the particle could be observed. We investigated the components at three different points, that is, at the center of particle, in the SEI layer, and on the reaction species (outside of the active particles). At the center of particle (point **1**), no obvious F is detected, and the pre-edge of O K-edge around 530 eV resulted from the hybridization of (Ni)Fe 3d−O 2p, which indicates that the large active particle is not fully reduced at the fully discharged state. In the SEI layer (point **2**), clear F K-edge shows up, a small shoulder (marked with a star) indicates the existence of LiF in the SEI layer.[32] Weak Fe L-edge is detected, and the disappearance of the pre-edge of O K-edge indicates the existence of Fe^0 in the SEI layer. At point **3**, only F K-edge is observed, which can be attributed to the electrolyte species, that is, $LiPF_6$. Furthermore, the high-resolution TEM image confirms the formation of Fe^0 nanocrystals embedded in the SEI (Figure 5c). XRD measurements were attempted before and after electrochemical cycling to determine the structure of the materials on the electrodes; however, the resolution of a lab source XRD is not optimal to interpret due to the strong effect of a sophisticated electrode, composed of the active materials, carbon, reaction products, and the current collector, etc., after cycling (Figure S5).

When the Ni−Fe−OH nanostructures underwent charging in the first cycle, that is, at the 50% charged and fully charged states, most of the nanostructures turned into irregularly shaped particles encapsulated by an SEI layer (Figures 6a, Figures S2 and S3). The STEM-EDS maps of the fully charged particle (Figure 6a) show that the SEI layer contains a considerable amount of F and P but a small amount of C and O. On the basis of this finding, and the characteristics of the F 1s XAS and O 1s XAS during cycling (Figure 4a,b), the SEI layer is likely dominated by fluorine species identified primarily as LiF. The STEM-EELS spectra of the active material particle (Figure 6b) show that the Fe L-edge is right-shifted from the particle center to the surface (~2 eV), consistent with a $Fe^0 \rightarrow Fe^{3+}$ transition during the charging process.[31] Accordingly, the pre-edge of the O K-edge shows up near the surface of the particle (marked with triangle in Figure 6b), and the LiF phase can still be found on the surface after charging (noted with a star in Figure 6b).

It is clear from the above analyses that the SEI layer plays a critical role in maintaining the good cyclability of the anode material (Figure 3b) in the lithium half-cell. Because of the existence of water molecules in the as-prepared Ni−Fe−OH nanostructures, the reaction of water with $LiPF_6$ could occur preferentially on the particle surface, which is given as[33,34]

$$LiPF_6 + H_2O \rightarrow LiF + POF_3 + 2HF$$

We expect this reaction is responsible for the observed LiF as a primary component of the SEI layer. Here, the controlled small fraction of water molecules in the as-synthesized hydroxide nanostructures contributes positively to maintain the good cyclability of the LIB anode. However, water is generally harmful to a battery system; the dehydrated material will be investigated for comparison in the future.

It is noted that the primary phase of LiF has also been identified in the SEI layer of graphite anode[35−37] and in the

DOI: 10.1021/cm5041375
Chem. Mater. 2015, 27, 1583−1589

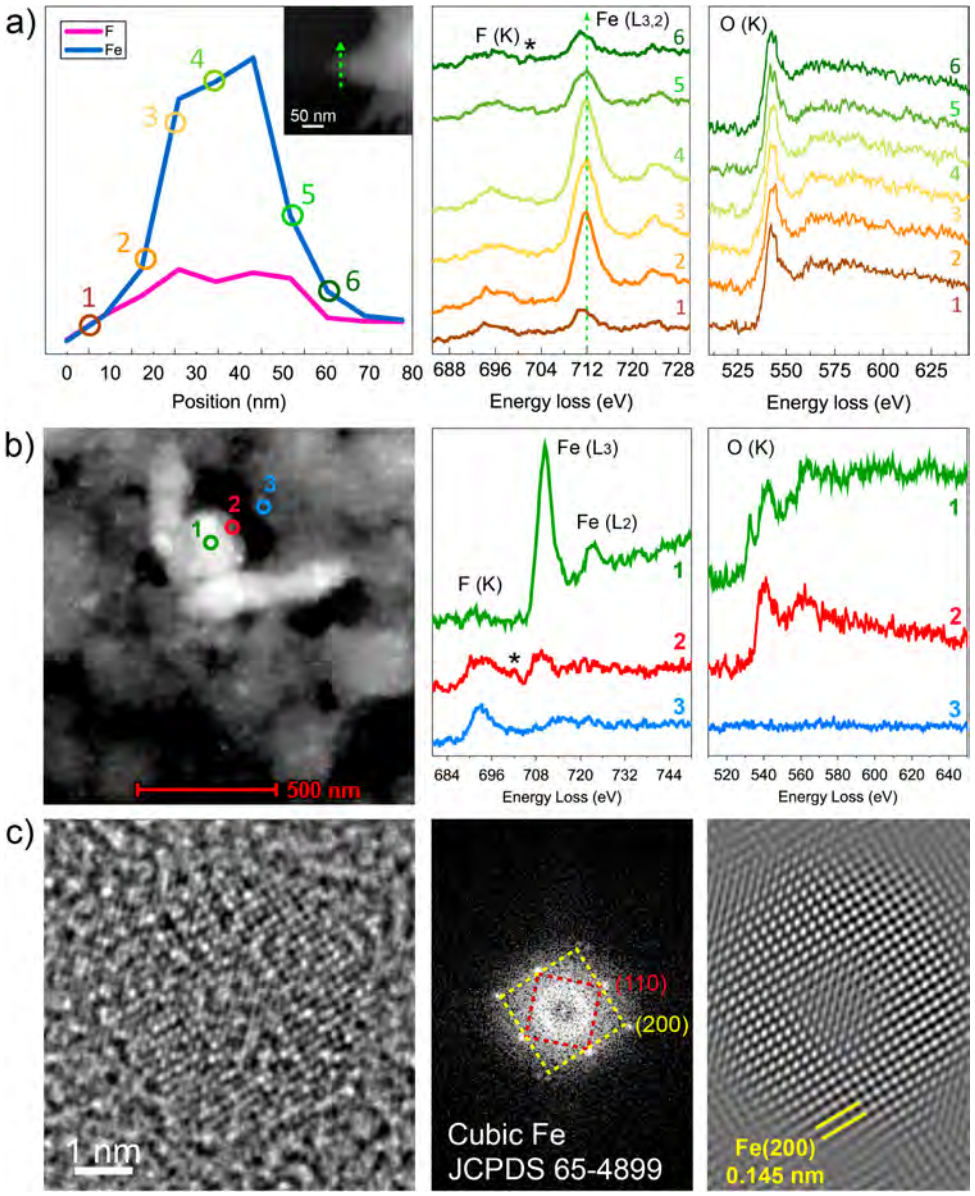

Figure 5. Structure of the active particles in the fully discharged state. (a) STEM image and EELS line scan profile over one nanostructure at the discharged state. The green dash arrow shows the EELS line scan pathway. The shoulder feature of LiF phase is marked with a star. (b) STEM image and EELS spectra at three different points on the image, where points **1**, **2**, and **3** are at the center of particle, in the SEI layer, and on the reaction species, respectively. (c) TEM image, fast Fourier transform (FFT) pattern, and inversed FFT image of the iron nanoparticle that is found on the surface of the large active particle.

surface reaction layers on $LiNi_xMn_xCo_{1-2x}O_2$ cathodes.[20] Because of the large band gap of LiF (~14 eV), the SEI impedes the transport of electrons through the layer while allowing lithium ions to pass through,[38−40] which prevents the continual decomposition of electrolyte below its thermodynamic reduction limit. As with graphite, this allows the hydroxide electrode to function reversibly even at low potentials (Figure 3b). As to the large capacity loss and irreversibility at the first a few cycles, this could be ascribed to the side reaction of the active materials with the electrolyte to form complex intermediates (Figure S4) and the incomplete redox reaction in the initial cycle (Figure 5b and Figure 6b), likely due to the protection of the SEI layer.

CONCLUSIONS

We synthesized amorphous nickel iron complex hydroxide nanostructures by a laser−chemical method, which showed improved lithium storage capability compared to other hydroxides. Complementary characterizations, including soft XAS and STEM-EELS/EDS, show that a SEI layer composed of a primary phase of LiF remains mostly intact on the surface of the active material particles during the charge/discharge processes, which plays a key role in maintaining repeated cycling of the electrode to low voltages. Incomplete redox reactions, formation of intermediate species, and pulverization of the active nanostructure were detected during the initial charge/discharge processes, which likely contributed to the irreversibility in the first several cycles. Further engineering of the SEI layer and of the active material based on the observations made here should result in further improvements

DOI: 10.1021/cm5041375
Chem. Mater. 2015, 27, 1583−1589

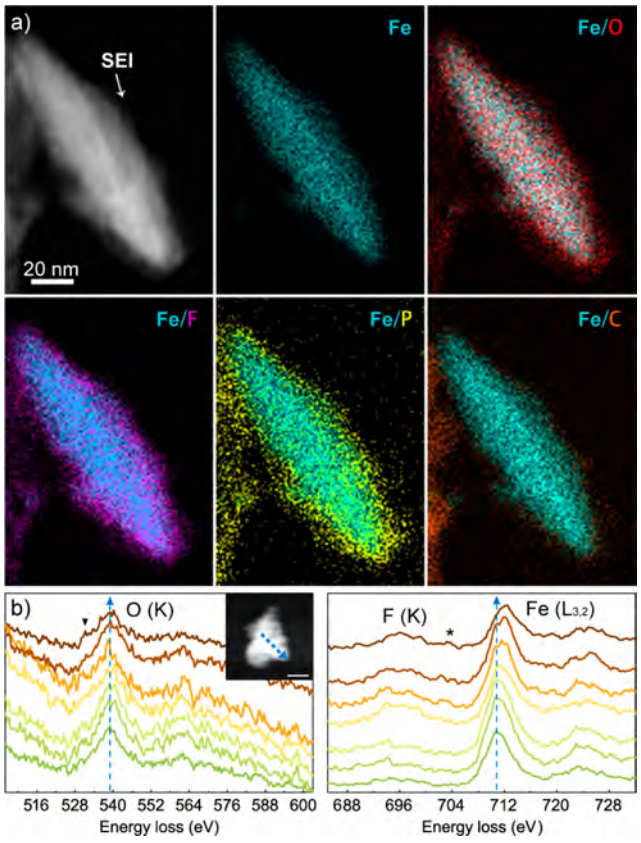

Figure 6. (a) STEM-EDS mapping of the Ni−Fe−OH nanostructure after one cycle. (b) EELS spectra of O K-edge and Fe L-edge across a Ni−Fe−OH particle after one cycle (charged). Inset is the STEM image of the particle, and the blue dashed arrow shows the path of EELS line scan. The scale bar is 50 nm. The triangle indicates the emergence of pre-edge of O K-edge and the star symbol marks the shoulder feature of LiF.

in performance, particularly in reducing Coulombic inefficiencies.

■ ASSOCIATED CONTENT

Supporting Information

Materials and methods, XAS of Ni oxidation states, EDS mapping of the active particles in 50% charged and fully charged states. This material is available free of charge via the Internet at http://pubs.acs.org.

■ AUTHOR INFORMATION

Corresponding Author

*E-mail: hmzheng@lbl.gov.

Author Contributions

‖K.N., F.L., and L.F. contributed equally.

Notes

The authors declare no competing financial interest.

■ ACKNOWLEDGMENTS

We used Tecnai and TitanX microscopes for structural analysis at the National Center for Electron Microscopy of Lawrence Berkeley National Laboratory (LBNL), which is supported by the U.S. Department of Energy Office of Basic Energy Sciences under Contract No. DE-AC02-05CH11231. The synchrotron X-ray portions of this research were carried out at the Stanford Synchrotron Radiation Lightsource (Beamlines 10-1 and 8-2), a directorate of SLAC National Accelerator Laboratory and an Office of Science User Facility operated for the U.S. Department of Energy Office of Science by Stanford University. L.F. acknowledges the support of the National Basic Research Program of China (2014CB931700), NSFC (Nos. 11074314, 11304405), and China Scholarship Council (CSC) under No. 2010850533. F.L., D.N., and T.-C.W. thank Dr. Jun-Sik Lee and Glen Kerr for the help at SSRL Beamline 8-2. H.Z. acknowledges the SinBeRise program of BEARS at University of California, Berkeley for travel support and the support of DOE Office of Science Early Career Research Program.

■ REFERENCES

(1) Arico, A. S.; Bruce, P.; Scrosati, B.; Tarascon, J.-M.; van Schalkwijk, W. *Nat. Mater.* **2005**, *4*, 366−377.
(2) Li, H.; Wang, Z.; Chen, L.; Huang, X. *Adv. Mater.* **2009**, *21*, 4593−4607.
(3) Liu, N.; Lu, Z.; Zhao, J.; McDowell, M. T.; Lee, H.-W.; Zhao, W.; Cui, Y. *Nat. Nanotechnol.* **2014**, *9*, 187−192.
(4) Poizot, P.; Laruelle, S.; Grugeon, S.; Dupont, L.; Tarascon, J. M. *Nature* **2000**, *407*, 496−499.
(5) Bruce, P. G.; Scrosati, B.; Tarascon, J.-M. *Angew. Chem., Int. Ed.* **2008**, *47*, 2930−2946.
(6) Hu, Y.-Y.; Liu, Z.; Nam, K.-W.; Borkiewicz, O. J.; Cheng, J.; Hua, X.; Dunstan, M. T.; Yu, X.; Wiaderek, K. M.; Du, L.-S.; Chapman, K. W.; Chupas, P. J.; Yang, X.-Q.; Grey, C. P. *Nat. Mater.* **2013**, *12*, 1130−1136.
(7) Wang, F.; Robert, R.; Chernova, N. A.; Pereira, N.; Omenya, F.; Badway, F.; Hua, X.; Ruotolo, M.; Zhang, R.; Wu, L.; Volkov, V.; Su, D.; Key, B.; Whittingham, M. S.; Grey, C. P.; Amatucci, G. G.; Zhu, Y.; Graetz, J. *J. Am. Chem. Soc.* **2011**, *133*, 18828−18836.
(8) Lin, F.; Nordlund, D.; Weng, T.-C.; Zhu, Y.; Ban, C.; Richards, R. M.; Xin, H. L. *Nat. Commun.* **2014**, *5*, 3358.
(9) Wang, H.; Cui, L.-F.; Yang, Y.; Sanchez Casalongue, H.; Robinson, J. T.; Liang, Y.; Cui, Y.; Dai, H. *J. Am. Chem. Soc.* **2010**, *132*, 13978−13980.
(10) Park, J. C.; Kim, J.; Kwon, H.; Song, H. *Adv. Mater.* **2009**, *21*, 803−807.
(11) Zhang, W.-M.; Wu, X.-L.; Hu, J.-S.; Guo, Y.-G.; Wan, L.-J. *Adv. Funct. Mater.* **2008**, *18*, 3941−3946.
(12) Wu, Z.-S.; Ren, W.; Wen, L.; Gao, L.; Zhao, J.; Chen, Z.; Zhou, G.; Li, F.; Cheng, H.-M. *ACS Nano* **2010**, *4*, 3187−3194.
(13) Zhou, G.; Wang, D.-W.; Yin, L.-C.; Li, N.; Li, F.; Cheng, H.-M. *ACS Nano* **2012**, *6*, 3214−3223.
(14) Zhang, G.; Lou, X. W. *Angew. Chem.* **2014**, *126*, 9187−9190.
(15) Cabana, J.; Monconduit, L.; Larcher, D.; Palacín, M. R. *Adv. Mater.* **2010**, *22*, E170−E192.
(16) Zhu, X.; Zhong, Y.; Zhai, H.; Yan, Z.; Li, D. *Electrochim. Acta* **2014**, *132*, 364−369.
(17) Li, B.; Cao, H.; Shao, J.; Zheng, H.; Lu, Y.; Yin, J.; Qu, M. *Chem. Commun.* **2011**, *47*, 3159−3161.
(18) Huang, X.-L.; Chai, J.; Jiang, T.; Wei, Y.-J.; Chen, G.; Liu, W.-Q.; Han, D.; Niu, L.; Wang, L.; Zhang, X.-B. *J. Mater. Chem.* **2012**, *22*, 3404−3410.
(19) He, Y.-S.; Bai, D.-W.; Yang, X.; Chen, J.; Liao, X.-Z.; Ma, Z.-F. *Electrochem. Commun.* **2010**, *12*, 570−573.
(20) Lin, F.; Markus, I. M.; Nordlund, D.; Weng, T.-C.; Asta, M. D.; Xin, H. L.; Doeff, M. M. *Nat. Commun.* **2014**, *5*, 3529.
(21) Lin, F.; Nordlund, D.; Weng, T.-C.; Sokaras, D.; Jones, K. M.; Reed, R. B.; Gillaspie, D. T.; Weir, D. G.; Moore, R. G.; Dillon, A. C. *ACS Appl. Mater. Interfaces* **2013**, *5*, 3643−3649.
(22) Yang, W.; Liu, X.; Qiao, R.; Olalde-Velasco, P.; Spear, J. D.; Roseguo, L.; Pepper, J. X.; Chuang, Y.-D.; Denlinger, J. D.; Hussain, Z. *J. Electron Spectrosc. Relat. Phenom.* **2013**, *190*, 64−74.
(23) Han, Y.; Liu, Z.-H.; Yang, Z.; Wang, Z.; Tang, X.; Wang, T.; Fan, L.; Ooi, K. *Chem. Mater.* **2007**, *20*, 360−363.
(24) Xu, L.; Ding, Y.-S.; Chen, C.-H.; Zhao, L.; Rimkus, C.; Joesten, R.; Suib, S. L. *Chem. Mater.* **2007**, *20*, 308−316.

DOI: 10.1021/cm5041375
Chem. Mater. 2015, 27, 1583−1589

(25) Liu, X.; Wang, D.; Liu, G.; Srinivasan, V.; Liu, Z.; Hussain, Z.; Yang, W. *Nat. Commun.* **2013**, *4*, 2568.
(26) Liu, X.; Liu, J.; Qiao, R.; Yu, Y.; Li, H.; Suo, L.; Hu, Y.-S.; Chuang, Y.-D.; Shu, G.; Chou, F.; Weng, T.-C.; Nordlund, D.; Sokaras, D.; Wang, Y. J.; Lin, H.; Barbiellini, B.; Bansil, A.; Song, X.; Liu, Z.; Yan, S.; Liu, G.; Qiao, S.; Richardson, T. J.; Prendergast, D.; Hussain, Z.; de Groot, F. M. F.; Yang, W. *J. Am. Chem. Soc.* **2012**, *134*, 13708−13715.
(27) van Aken, P. A.; Liebscher, B.; Styrsa, V. J. *Phys. Chem. Miner.* **1998**, *25*, 494−498.
(28) De Groot, F.; Grioni, M.; Fuggle, J.; Ghijsen, J.; Sawatzky, G.; Petersen, H. *Phys. Rev. B* **1989**, *40*, 5715.
(29) Hudson, E.; Moler, E.; Zheng, Y.; Kellar, S.; Heimann, P.; Hussain, Z.; Shirley, D. *Phys. Rev. B* **1994**, *49*, 3701.
(30) Qiao, R.; Chuang, Y.-D.; Yan, S.; Yang, W. *PLoS One* **2012**, *7*, e49182.
(31) Tan, H.; Verbeeck, J.; Abakumov, A.; Van Tendeloo, G. *Ultramicroscopy* **2012**, *116*, 24−33.
(32) Al-Sharab, J. F.; Bentley, J.; Badway, F.; Amatucci, G. G.; Cosandey, F. *J. Nanopart. Res.* **2013**, *15*, 1−12.
(33) Aurbach, D.; Zaban, A.; Ein-Eli, Y.; Weissman, I.; Chusid, O.; Markovsky, B.; Levi, M.; Levi, E.; Schechter, A.; Granot, E. *J. Power Sources* **1997**, *68*, 91−98.
(34) Heider, U.; Oesten, R.; Jungnitz, M. *J. Power Sources* **1999**, *81*, 119−122.
(35) Xiao, A.; Yang, L.; Lucht, B. L.; Kang, S.-H.; Abraham, D. P. *J. Electrochem. Soc.* **2009**, *156*, A318−A327.
(36) Wang, F.; Graetz, J.; Moreno, M. S.; Ma, C.; Wu, L.; Volkov, V.; Zhu, Y. *ACS Nano* **2011**, *5*, 1190−1197.
(37) Nie, M.; Chalasani, D.; Abraham, D. P.; Chen, Y.; Bose, A.; Lucht, B. L. *J. Phys. Chem. C* **2013**, *117*, 1257−1267.
(38) Chen, Z.; Ren, Y.; Jansen, A. N.; Lin, C.-K.; Weng, W.; Amine, K. *Nat. Commun.* **2013**, *4*, 1513.
(39) Li, C.; Gu, L.; Maier, J. *Adv. Funct. Mater.* **2012**, *22*, 1145−1149.
(40) Lu, Y.; Tu, Z.; Archer, L. A. *Nat. Mater.* **2014**, *13*, 961−969.

DOI: 10.1021/cm5041375
Chem. Mater. 2015, 27, 1583−1589